


# *In-situ* measurement of cell temperature by spin-relaxation rate analysis for an atomic magnetometer

Bing-Quan Zhao(赵丙权), Zhe Qi(祁喆), Jian-Long Wang(王建龙), Li-Hua Wu(武丽花), Qian-Yun Zhao(赵倩云), Jun-Xin Wei(韦俊新), Wei-Ren Liu(刘为任), and Ling-Xin Kong(孔令鑫)

**Citation:**Chin. Phys. B, 2026, 35 (**6**): 060703. DOI: 10.1088/1674-1056/ae07bf
http://cpb.iphy.ac.cn; http://iopscience.iop.org/cpb

**What follows is a list of articles you may be interested in**

---

## Realization of an optimized cylindrical uniform magnetic field coil via flexible printed circuit technology

A-Hui Zhao(赵阿慧), Yong-Le Zhang(张永乐), Yue-Yue Liang(梁跃跃), Yi Zhang(张艺), Jun-Jun Zha(查君君), Dao-Rong Rui(芮道荣), Xiao-Qiang Zhang(张肖强), and Kang Yang(杨康)

Chin. Phys. B, 2024, 33 (**12**): 120702. DOI: 10.1088/1674-1056/ad84c1

## Performance optimization of a SERF atomic magnetometer based on flat-top light beam

Ziqi Yuan(袁子琪), Junjian Tang(唐钧剑), Shudong Lin(林树东), and Yueyang Zhai(翟跃阳)

Chin. Phys. B, 2024, 33 (**6**): 060703. DOI: 10.1088/1674-1056/ad401b

## Response optimization of a three-axis sensitive SERF magnetometer for closed-loop operation

Yuanrui Zhou(周原锐), Yongze Sun(孙永泽), Xixi Wang(汪茜茜), Jianan Qin(秦佳男), Xue Zhang(张雪), and Yanzhang Wang(王言章)

Chin. Phys. B, 2024, 33 (**2**): 020701. DOI: 10.1088/1674-1056/ad0b00

## A compact and closed-loop spin-exchange relaxation-free atomic magnetometer for wearable magnetoencephalography

Qing-Qian Guo(郭清乾), Tao Hu(胡涛), Xiao-Yu Feng(冯晓宇), Ming-Kang Zhang(张明康), Chun-Qiao Chen(陈春巧), Xin Zhang(张欣), Ze-Kun Yao(姚泽坤), Jia-Yu Xu(徐佳玉),Qing Wang(王青), Fang-Yue Fu(付方跃), Yin Zhang(张寅), Yan Chang(常严), and Xiao-Dong Yang(杨晓冬)

Chin. Phys. B, 2023, 32 (**4**): 040702. DOI: 10.1088/1674-1056/ac7e38

## Dynamic range and linearity improvement for zero-field single-beam atomic magnetometer

Kai-Feng Yin(尹凯峰), Ji-Xi Lu(陆吉玺), Fei Lu(逯斐), Bo Li(李博), Bin-Quan Zhou(周斌权), and Mao Ye(叶茂)

Chin. Phys. B, 2022, 31 (**11**): 110703. DOI: 10.1088/1674-1056/ac6010

---

# *In-situ* measurement of cell temperature by spin-relaxation rate analysis for an atomic magnetometer

Bing-Quan Zhao(赵丙权)[1,2], Zhe Qi(祁喆)[2,†], Jian-Long Wang(王建龙)[2], Li-Hua Wu(武丽花)[2], Qian-Yun Zhao(赵倩云)[2], Jun-Xin Wei(韦俊新)[2], Wei-Ren Liu(刘为任)[2], and Ling-Xin Kong(孔令鑫)[3,‡]

[1] *College of Intelligent Systems Science and Engineering, Harbin Engineering University, Harbin* 150006, *China*
[2] *Tianjin Key Laboratory of Quantum Precision Measurement Technology, Tianjin Navigation and Instrument Institute, Tianjin* 300131, *China*
[3] *Optical Fiber-Based Intelligent Sensing and Micromachines Laboratory, Yantai University, Yantai* 264005, *China*

(Received 18 June 2025; revised manuscript received 15 August 2025; accepted manuscript online 17 September 2025)

Alkali-metal vapor cells are the core sensing components of atomic magnetometers. To achieve high-sensitivity magnetic field measurements, the cells require heating and stabilization at high temperatures. Here, we propose an *in-situ* temperature measurement method for a vapor cell of an atomic magnetometer based on spin-relaxation analysis. This technique establishes a direct functional correlation between the cell temperature and the spin-relaxation rate under low pumping power conditions. Experimental validation within the temperature range of 90 °C–130 °C confirms the accuracy of this approach. We further investigate the effects of magnetic fields on measurement precision and demonstrate the long-term, high-precision capabilities of temperature detection. This non-invasive technique presents a critical advantage for precise thermal optimization of atomic magnetometers.

**Keywords:** atomic magnetometer, *in-situ* measurement, spin exchange, atomic number density

**PACS:** 07.07.Df, 07.55.Ge, 33.35.+r

**DOI:** 10.1088/1674-1056/ae07bf **CSTR:** 32038.14.CPB.ae07bf

## 1. Introduction

Magnetic field measurement serves as a critical technology in diverse domains, including biomagnetism,[1–4] mineral exploration,[5–7] navigation,[8,9] and fundamental physics.[10–12] Among various sensing techniques, atomic magnetometers based on the detection of Larmor spin precession of optically pumped atoms have emerged as the most promising magnetic sensors, owing to their ultrahigh sensitivity[13–17] and sub-millimeter spatial resolution.[18,19]

The vapor cell containing a small amount of alkali metal atoms is the core component of atomic magnetometers. To enhance signal strength and stability, a closed-loop heating system is employed to maintain an elevated and precisely controlled atomic density. This system typically consists of a temperature sensor (*e.g.*, a thermocouple or resistance-temperature detector) and a feedback-controlled heater.[20,21] However, the inevitable magnetic interference generated by conventional temperature sensors degrades the sensitivity of atomic magnetometers. Furthermore, these sensors are hard to measure the internal temperature due to the sealed cell. In recent years, several studies have been conducted on *in-situ* cell temperature measurement. The light absorption methods[22–24] have been successfully employed to quantify the atomic density number in cells and enable closed-loop temperature control for SERF magnetometers.[25] Furthermore, through steady-state linewidth analysis, the internal temperature of the vapor cell in a pump–probe configured magnetometer can be determined.[26] However, these studies have yet to establish a definitive correlation between cell temperature and spin-relaxation rates. More critically, the impact of magnetic fields on thermal measurement accuracy remains insufficiently investigated, which compromises measurement precision in practical applications.

In this study, we present a method for measuring the vapor cell temperature in a single-beam atomic magnetometer. Under the spin exchange relaxation dominated regime, we derive a quantitative dependence between the transverse relaxation rate and cell temperature. Experiments are conducted in the temperature range of 90 °C to 130 °C to validate the method, and the influence of magnetic fields is systematically studied. The results show that our approach achieves a 1% relative deviation compared to reference sensor measurements. The proposed setup achieves significant simplification by requiring only a single circularly-polarized light source, rendering it ideally suited for compact magnetometers.[27,28]

## 2. Principle

The basic principle of the scalar magnetometer relies on the interaction between the magnetic field and the atomic spins. A circularly polarized laser resonant with the $^{87}$Rb D1

†Corresponding author. E-mail: 1120170088@mail.nankai.edu.cn
‡Corresponding author. E-mail: 1120170096@mail.nankai.edu.cn

© 2026 Chinese Physical Society and IOP Publishing Ltd. All rights, including for text and data mining, AI training, and similar technologies, are reserved.

transition transfers its angular momentum to the ensemble of atoms. Polarized atoms in an external magnetic field precess at the Larmor frequency, which is dependent on the magnetic field. The evolution of the spin polarization can be described by the Bloch equation[29,30]

$$\dot{\boldsymbol{S}} = \gamma \boldsymbol{B} \times \boldsymbol{S} - \frac{S_x \hat{x} + S_y \hat{y}}{T_2} - \frac{(S_z - S_0)\hat{z}}{T_1}, \tag{1}$$

where $\boldsymbol{S}$ is the polarization vector and $S_0$ is the equilibrium spin polarization in the absence of all magnetic fields. $\boldsymbol{B}$ is the total magnetic field vector including a radio frequency magnetic field $\boldsymbol{B}_{\rm rf}$ and a static magnetic field $\boldsymbol{B}_0$, $\gamma$ is the gyromagnetic ratio. $T_1$ and $T_2$ are the longitudinal relaxation time and transverse relaxation time, respectively. Figure 1 illustrates the directions of $\boldsymbol{B}_0$, $\boldsymbol{B}_{\rm rf}$, and light propagation, with $\theta$ defined as the angle between $\boldsymbol{B}_0$ and the wave vector $\boldsymbol{k}$.

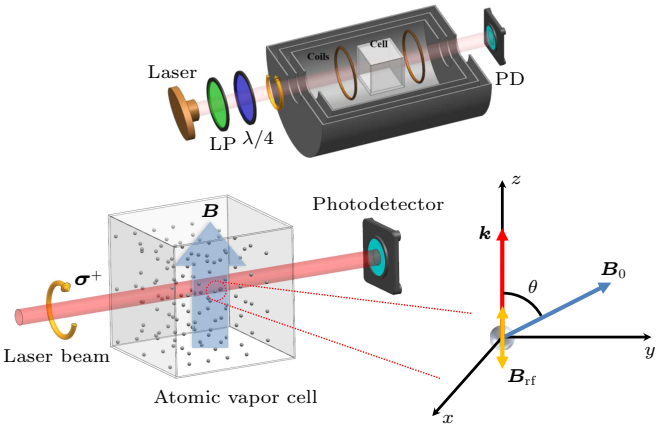



**Fig. 1.** Principle of an atomic magnetometer. The directions of the magnetic field and light propagation are specified. LP: linear polarizer, $\lambda/4$: quarter-wave plate.

The transverse relaxation time $T_2$ is given by the rates of the various mechanisms that cause dephasing between precessing atoms,[31]

$$\frac{1}{T_2} = \frac{1}{q}\left(R_{\rm rel} + R_{\rm op}\right) + \frac{1}{q_{\rm se}} R_{\rm se} + R_{\rm gr}, \tag{2}$$

where $R_{\rm op}$ is the optical pumping rate, which is proportional to the light intensity.[32] $R_{\rm se}$ is the spin-exchange relaxation rate, $R_{\rm rel}$ is the relaxation rate due to other collisions, $R_{\rm gr}$ is the rate of relaxation due to magnetic field gradient. $q$ is the slowing-down factor, which relies on the polarization. The spin-exchange broadening factor $q_{\rm se}$ depends on the ambient magnetic field and the alkali vapor density.

The $T_2$ measurements can be carried out through different methods.[33,34] Here, we obtain $T_2$ by the fitting-ratio method.[35] The phase shift $\varphi$ of the light power with respect to the driving magnetic field $\boldsymbol{B}_{\rm rf}$ is

$$\varphi = \arctan\left(\frac{T_2^{-1}}{\omega - \omega_0}\right), \tag{3}$$

where $\omega$–$\omega_0$ is the frequency detuning from the Larmor frequency $\omega_0$. Usually, $R_{\rm se}$ is much larger than any other spin-relaxation mechanism.[36] With a low pump beam intensity, the expression for the transverse relaxation time $T_2$ is simplified:

$$\frac{1}{T_2} \approx \frac{1}{q_{\rm se}} R_{\rm se} = \frac{1}{q_{\rm se}} \left(n_{\rm alk} \times \sigma_{\rm se} \times \bar{v}\right), \tag{4}$$

where $\sigma_{\rm se}$ is the alkali–alkali spin-exchange cross-section, $\sigma_{\rm se} = 1.9 \times 10^{-14}$ cm$^{-2}$ for $^{87}$Rb atoms.[37] The relative thermal velocity $\bar{v} = \sqrt{8k_{\rm B}T/\pi M}$, $k_{\rm B}$ is the Boltzmann constant, $T$ is the temperature in Kelvin, and $\frac{1}{M} = \frac{1}{m_{\rm A}} + \frac{1}{m_{\rm B}}$ is the reduced mass of the two alkali metal atoms A and B, given by the masses $m_{\rm A}$ of the alkali atom and $m_{\rm B}$ of the perturber. Thus, the relationship between the transverse relaxation time $T_2$ and the corresponding saturated density $n_{\rm alk}$ is

$$n_{\rm alk} = \frac{q_{\rm se}}{T_2 \times \sigma_{\rm se} \times \bar{v}}. \tag{5}$$

The saturated density of the alkali vapor in units of cm$^{-3}$ at a Kelvin temperature $T$ is given by the equation[38]

$$n_{\rm alk} = \frac{1}{T} 10^{21.866 + A - B/T}, \tag{6}$$

for rubidium in the liquid phase, $A = 4.312$, $B = 4040$. By combining Eqs. (5) and (6), the temperature $T$ can be expressed as a function of the transverse relaxation rate $T_2^{-1}$

$$T = \frac{-2B\ln(10)}{W\left(-2B\ln(10) \times 10^{-2b} \times \left(aT_2^{-1}\right)^2\right)}, \tag{7}$$

$$a = \frac{q_{\rm se}}{\sigma_{\rm se} \times \sqrt{8k_{\rm B}/\pi M}}, \tag{8}$$

$$b = 21.866 + A, \tag{9}$$

where $W(z)$ is the Lambert $W$-function, $a$ and $b$ are the parameters. Details on the derivation of Eq. (7) are provided in Supporting information. Once the relaxation rate is determined, the temperature of the atomic cell can be derived from Eq. (7). The validity of the proposed method is confirmed through subsequent experiments and simulations.

## 3. Experimental design and configuration

We use the single-beam configuration shown in Fig. 2. A cubical alkali metal cell with a 20-mm length is filled with a droplet of $^{87}$Rb atoms and 700 Torr (1 Torr = $1.33322 \times 10^2$ Pa) of nitrogen. It is placed inside a boron nitride oven with four symmetrically arranged heating wires and heated by an alternating current heating device. A Pt1000 temperature sensor affixed to the cell is used to monitor the setting temperature. The triaxial coils are mounted to apply the oscillating magnetic field and bias magnetic field, respectively. A four-layer cylindrical magnetic shield is utilized to isolate the external magnetic field.

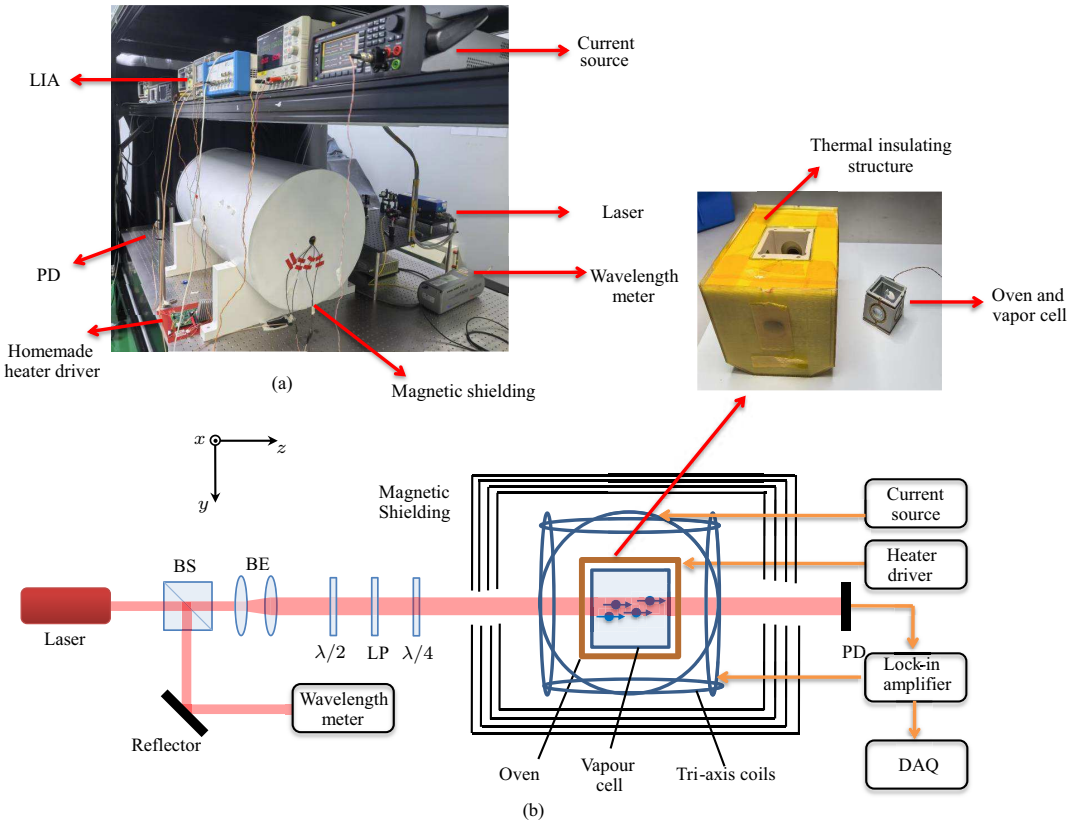



**Fig. 2.** Photograph (a) and schematic diagram (b) of the experimental setup. A circularly polarized light propagates along the $z$-axis, and the transmitted light intensity is detected by the photodetector behind the vapor cell. The outer layer of the cell and oven is a thermal insulation structure, located in a multilayer magnetic shield to suppress external field fluctuation. BS: beam splitter, BE: beam expander, $\lambda/2$: half-wave plate, LP: linear polarizer, $\lambda/4$: quarter-wave plate, PD: photodetector.

The laser beam propagating along the $z$-axis is tuned to 794.9989 nm. After passing through a linear polarizer and a quarter-wave plate in sequence, this beam transforms into circularly polarized light. The transmitted beam through the vapor cell is collected by a photodiode. The converted light signal is then sent to a lock-in amplifier (Zurich Instruments MFLI) to measure the phase shift of the photocurrent with respect to the driving magnetic field. A uniform static magnetic field of 7.15 μT, generated by a current source, is applied in the $YZ$-plane at 45° to the $z$-axis. Simultaneously, an oscillating magnetic field with an amplitude of 13.2 nT, generated by the lock-in amplifier output, is applied along the $z$-axis, with its frequency $\omega$ swept across the Larmor frequency.

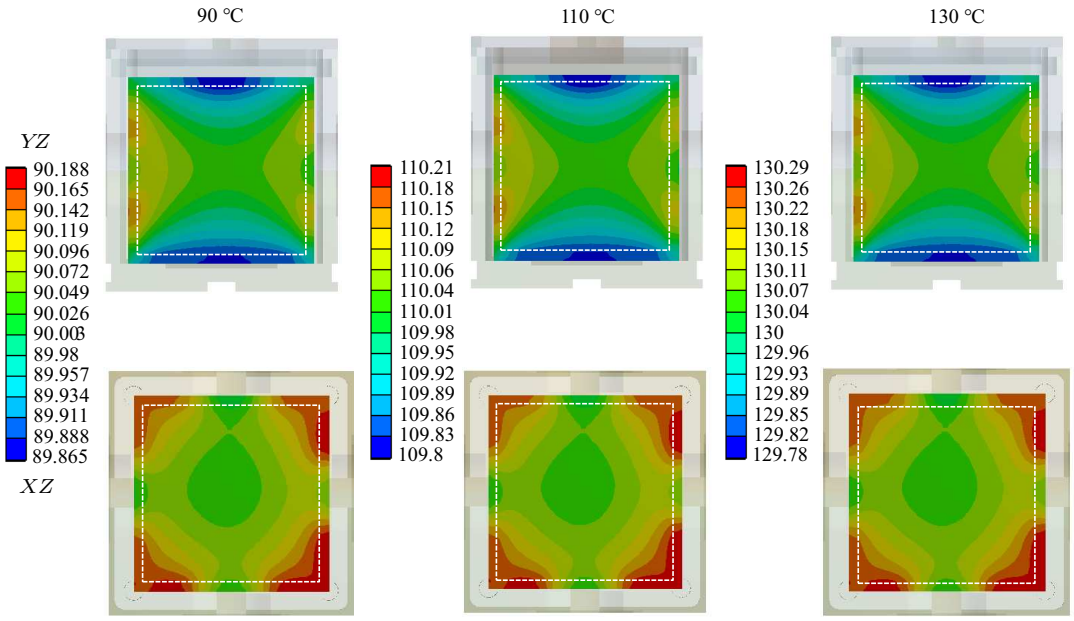



**Fig. 3.** Simulation results of the steady-state temperature distribution of the cell. White dashed lines delineate the cell's inner surfaces. The $YZ$ plane lies perpendicular to the experimental platform, while the $XZ$ plane lies parallel to it.

Using ANSYS Workbench, we simulate thermally steady states of the vapor cell at various temperatures. As shown in Fig. 3, where white dashed lines indicate the cell's inner surfaces, the *XZ* plane bisects the cell parallel to the horizontal plane, while the *YZ* plane bisects it perpendicularly. Temperature distributions reveal cold zones near access holes, contrasting with heat concentration around heating wires in the *XZ* plane, whereas the *YZ* plane exhibits low-temperature regions near the upper and lower surfaces. These findings indicate that optimal thermistor placement requires positioning near the cell's outer surface while maintaining adequate distance from both access holes and heating wires to ensure temperature measurements accurately reflect internal conditions. Additionally, to minimize measurement bias induced by spatial temperature heterogeneity, a thermal equilibrium waiting period exceeding 40 minutes is implemented after initial temperature stabilization in all experiments.

## 4. Results and discussion

According to Eq. (4), we first determine the light power used in the experiment. The oscillating magnetic field is generated via coils controlled by the reference output of the lock-in amplifier. The vapor cell temperature is set to 100 °C. As the driving frequency is swept from 49 kHz to 52 kHz, the phase shift between the photodiode output and the driving magnetic field is measured. In Fig. 4(a), the magnitude of the phase signal and frequency detuning are fitted by Eq. (3) to obtain the relaxation rate $T_2^{-1}$. As shown in Fig. 4(b), the total relaxation rate decays progressively and approaches 230 Hz with reduced optical pumping intensity. When the light intensity falls below 25 μW, the signal-to-noise ratio (SNR) of the phase signal is further reduced, leading to an inaccurate $T_2$ value extracted via fitting. Therefore, the incident optical power is set at 25 μW.

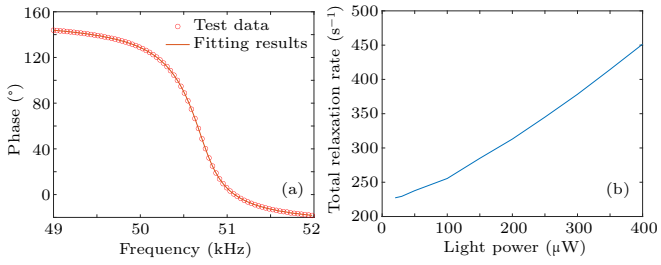



**Fig. 4.** Experimental data and fitting curve by scanning the frequency $\omega$ of the oscillating magnetic field. (a) The relative phase shift between the oscillating magnetic field and the modulated optical transmission signal. The circles and solid curve are test data and fitting results, respectively. (b) Experimentally evaluated $T_2^{-1}$ as a function of the light intensity.

The atomic density numbers and corresponding vapor cell temperatures are shown in Figs. 5(a) and 5(b), respectively. When the temperature varies from 90 °C to 130 °C, the atomic density numbers estimated from the saturated vapor pressure equation and the transverse relaxation rate exhibit close agreement. Due to the consistency of the atomic density numbers, the validity of the temperature calculation based on the relaxation rate analysis can be expected. Figure 5(b) compares temperatures acquired through conventional sensor measurements (blue circles) and the proposed method (red triangles). The agreement between these data validates the accuracy of our approach.

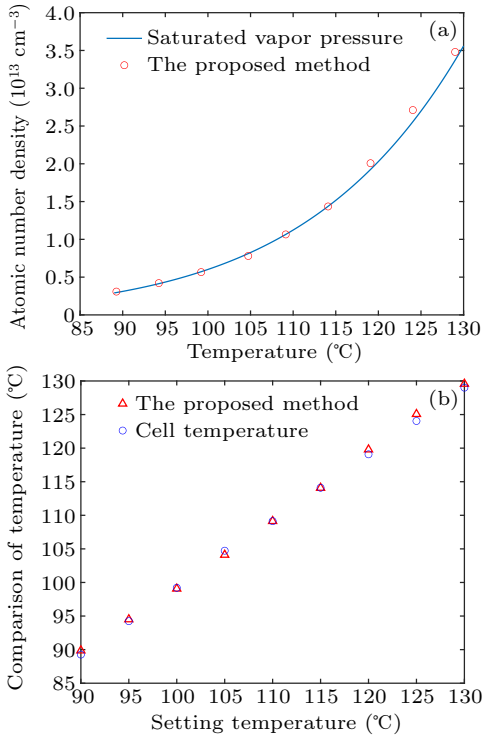



**Fig. 5.** Verification of atomic number density and corresponding temperature. The temperature range spans from 90 °C to 130 °C. (a) Theoretical predictions of the atomic density numbers are calculated from the saturated vapor pressure (solid line) and the proposed method (red circles), respectively. (b) Comparisons between the cell temperature measured by temperature detectors (blue circles) and the one estimated based on relaxation rate analysis (red triangles).

We then evaluate the influence of magnetic field amplitude variations on temperature measurement. Experiments are performed at 99.19 °C and 109.13 °C, respectively. Both temperature and relaxation rate exhibit similar trends as the magnetic field varies. In Fig. 6(a), the variation range of the oscillating magnetic field is set as 13.2 nT to 66 nT. The enhanced amplitude of the oscillating magnetic field induces an elevation of the obtained temperature. This occurs since the larger oscillating amplitudes lead to an increase in the relaxation rate, as shown in Fig. 6(b). The amplitude should therefore be chosen to enable an enhanced signal without greatly affecting the relaxation rate. Figure 6(c) illustrates that a similar trend of theoretical temperature exists when the static magnetic field increases. The primary mechanism arises from the amplified magnetic field gradient across the vapor cell under stronger magnetic field conditions. This heightened gradient renders the $R_{gr}$ non-negligible, thereby violating the approximation validity established in Eq. (4). Experimental data in Fig. 6(d) demonstrate a consistent increase in the relaxation rate with rising static magnetic fields (from 7.15 μT to 35.7 μT) at different temperatures.

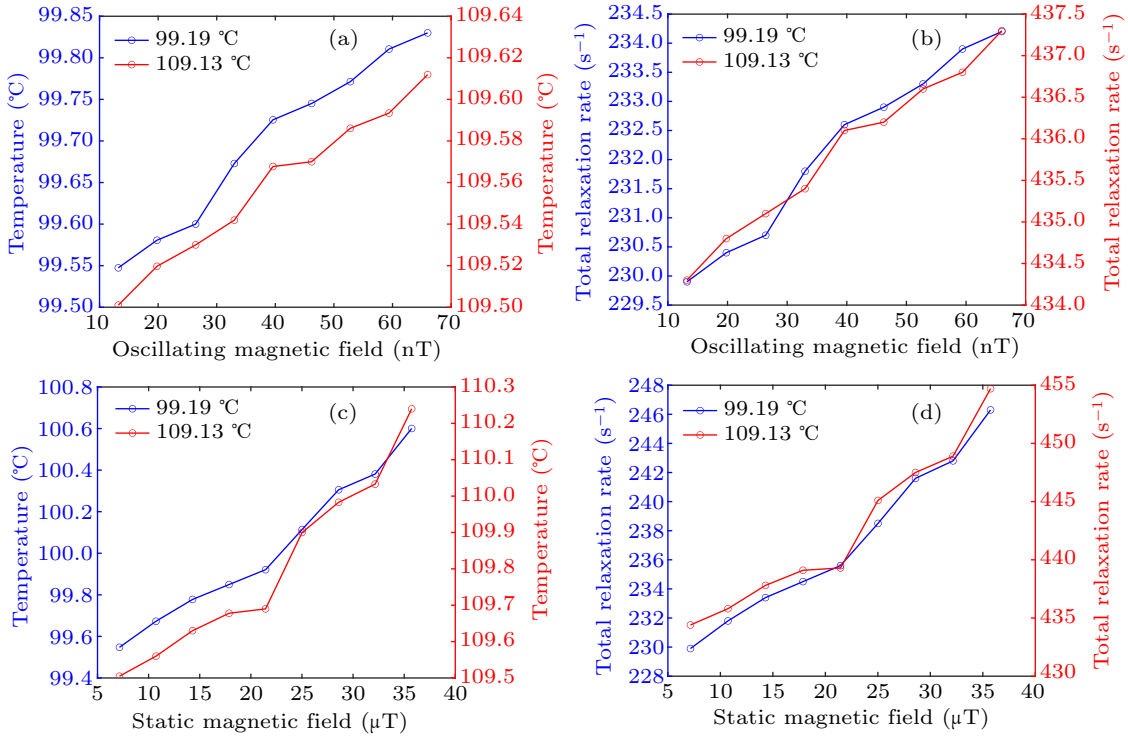



**Fig. 6.** Effects of (a) oscillating and (c) static magnetic field on temperature estimation. The corresponding total relaxation rates are plotted as a function of the magnetic field in subfigures (b) and (d), respectively. The experiments are conducted under two temperature conditions: the red curve shows results at 99.19 °C and the blue curve shows results at 109.13 °C.

To illustrate the reliability and accuracy of the proposed approach, Table 1 compares the monitored cell temperatures with the predictions based on relaxation rate analysis. Setting temperatures of 100 °C, 110 °C, and 120 °C are applied, while the actual temperatures are monitored using the sensor. Each cell temperature value represents the average over 50 sampling points. Experimental results demonstrate a $\leq 1\%$ relative deviation from the cell temperature reference values. Since the spin-exchange relaxation is approximated by the measured total spin relaxation rate, the calculated temperature is systematically overestimated, generating a consistent positive bias.

**Table 1.** The comparison between the measured temperature and the one obtained from the proposed method.

| Cell Temperature (°C) | The proposed method (°C) | Relative deviation (%) |
|---|---|---|
| 99.198 | 99.52 | 0.324 |
| 99.185 | 99.51 | 0.327 |
| 99.187 | 99.54 | 0.355 |
| 109.123 | 109.5 | 0.345 |
| 109.122 | 109.56 | 0.401 |
| 109.125 | 109.74 | 0.563 |
| 119.064 | 119.98 | 0.769 |
| 119.065 | 120 | 0.785 |
| 119.065 | 119.98 | 0.768 |

Figure 7 shows the continuous temperature measurement results. The blue curve represents the temperature fluctuations measured by the sensor, and the red curve represents the calculation results using the given method. The cell temperature fluctuates around 99.18 °C, while the calculated temperature is approximately 99.5 °C. Long-term temperature measurement data remain stable, with the relative error maintained at approximately 0.32%. We note that the calculated results are slightly higher than the cell temperature. This discrepancy originates from the measured total relaxation rate $T_2^{-1}$ exceeding the spin exchange relaxation rate $R_{se}$. This deviation consequently amplifies the computational output of Eq. (7).

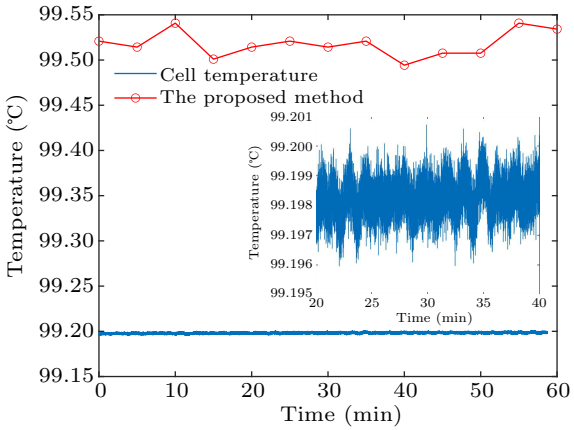



**Fig. 7.** Results of continuous temperature monitoring over one hour. The red curve depicts calculated values, while the blue curve shows actual sensor measurements. The insert plot represents continuous temperature measurements recorded over 20 minutes.

## 5. Conclusion and perspectives

In summary, this study presents an *in-situ* temperature measurement method for single-beam optically pumped magnetometers through relaxation rate analysis. A general expression relating the vapor cell temperature to the spin-relaxation rate is derived and verified. The relaxation rate is obtained un-

der low pumping power conditions to ensure the dominance of the spin-exchange relaxation. This monitoring method coincides well with the density saturated vapor pressure curve and the actual temperature recorded by a Pt1000. We analyzed the influence of the oscillating magnetic field and the static magnetic field experimentally. The magnetic field amplitudes should be moderate to suppress other relaxation mechanisms that amplify the total spin relaxation rate beyond the spin-exchange-dominated regime. The proposed model achieves $\leq$1% relative deviation between reference sensor measurements and computational predictions in the temperature range of 100 °C to 120 °C. The developed method can also be applied to temperature optimization and regulation for other alkali-metal magnetometers.

## Acknowledgements

Project supported by the National Natural Science Foundation of China (Grant No. 62105278), the Natural Science Foundation of Shandong Province, China (Grant No. ZR2021QF139), and Qingchuang Technology Support Program of University in Shandong Province, China (Grant No. 2024KJG040).

## References

[1] Jia L, Li J L, Song X D, Qi S J, Long T Y, Wu Z D, Wang R N and Ning X L 2025 *IEEE Trans. Instrum. Meas.* **74** 1
[2] Roth B J 2023 *Sensors* **23** 4218
[3] Kim Y J, Chu P H and Savukov I 2018 *Phys. Rev. Lett.* **121** 091802
[4] Yang Y F, Xu M Z, Liang A M, Yin Y, Ma X, Gao Y and Ning X L 2021 *Sci. Rep.* **11** 5564
[5] Adagunodo T, Sunmonu L and Adeniji A 2020 *Nat. Resour. Res.* **29** 521
[6] Perikleous D, Margariti K, Velanas P, Blazquez C S, Garcia P C and Gonzalez-Aguilera D 2024 *Drones* **9** 24
[7] Okada K 2022 *Miner. Econ.* **35** 429
[8] Sreevidya P, Khan J, Barshilia H C, Ananda C and Chowdhury P 2018 *J. Magn. Magn. Mater.* **448** 298
[9] Nam J, Lee W, Jung E and Jang G 2017 *IEEE T. Ind. Electron.* **65** 5673
[10] Afach S, Buchler B C, Budker D, Dailey C, Derevianko A, Dumont V, Figueroa N L, Gerhardt I, Grujić Z D and Guo H 2021 *Nat. Phys.* **17** 1396
[11] Bloch I M and Kalia S 2024 *J. High Energy Phys.* **2024** 178
[12] Alonso R, Blas D and Wolf P 2019 *J. High Energy Phys.* **2019** 69
[13] Xiao W, Liu M, Wu T, Peng X and Guo H 2023 *Phys. Rev. Lett.* **130** 143201
[14] Meng X, Zhang Y W, Zhang X C, Jin S C, Wang T R, Jiang L, Xiao L T, Jia S T and Xiao Y H 2023 *Nat. Commun.* **14** 6105
[15] Li W H, Peng X, Budker D, Wickenbrock A, Pang B, Zhang R and Guo H 2017 *Opt. Lett.* **42** 4163
[16] Guo Q Q, Hu T, Feng X Y, Zhang M K, Chen C Q, Zhang X, Yao Z K, Xu J Y, Wang Q, Fu F Y, Zhang Y, Chang Y and Yang X D 2023 *Chin. Phys. B* **32** 040702
[17] Zhou Y R, Sun Y Z, Wang X X, Qin J N, Zhang X and Wang Y Z 2024 *Chin. Phys. B* **33** 020701
[18] Fang X J, Wei K, Zhao T, Zhai Y Y, Ma D Y, Xing B Z, Liu Y and Xiao Z S 2020 *Opt. Express* **28** 26447
[19] Liu C, Dong H F and Sang J J 2021 *Appl. Phys. Lett.* **119** 114002
[20] Li J D, Quan W, Zhou B Q, Wang Z, Lu J X, Hu Z H, Liu G and Fang J C 2018 *IEEE Sens. J.* **18** 8198
[21] Lucivero V, Lee W, Dural N and Romalis M 2021 *Phys. Rev. Appl.* **15** 014004
[22] Ito Y, Ohnishi H, Kamada K and Kobayashi T 2012 *AIP Adv.* **2** 032127
[23] Li R J, Quan W and Fang J C 2017 *IEEE Photonics J.* **9** 6
[24] Yin Y, Zhou B Q, Yin K F, Wang Y X, Tang J J, Ye M, Ning X L and Han B C 2021 *J. Phys. D: Appl. Phys.* **54** 485001
[25] Liu Z, Lu J X, Yan Y G, Zhan D, Wang W Y, Li X Y and Li J L 2023 *Meas. Sci. Technol.* **34** 085108
[26] Zhang H, Zou S, Quan W and Chen X Y 2024 *Sensor. Actuat. A: Phys.* **379** 115900
[27] Li J J, Fang X J, Li R J, Chen B D, Zhai Y Y and Liu Y 2023 *Chin. Phys. B* **32** 053201
[28] Kurian K G, Sahoo S S, Madhu P K and Rajalakshmi G 2023 *Phys. Rev. Appl.* **19** 054040
[29] Wang W Y, Xia M M, Quan W and Wei K 2024 *Quantum Sci. Technol.* **9** 035048
[30] Zhu J, Jiang L W, Zhao X, Liu J L, Fang C, Shao Q, Zou Y T, Xu J H and Wang Z 2025 *Measurement* **242** 115983
[31] Seltzer S J *Developments in alkali-metal atomic magnetometry* (Princeton University) p. 51
[32] Appelt S, Baranga A B A, Young A and Happer W 1999 *Phys. Rev. A* **59** 2078
[33] Jia L, Song X D, Li J L, Suo Y C, Yang C X, Long T Y and Ning X L 2023 *IEEE Sens. J.* **23** 12988
[34] Wei M M, Yu W B, Zhou M, Huang W, Liu Y and Xu X 2023 *AIP Adv.* **13** 035327
[35] Terao A, Ban K, Ichihara S, Mizutani N and Kobayashi T 2013 *Phys. Rev. A* **88** 063413
[36] Savukov I M, Seltzer S, Romalis M and Sauer K 2005 *Phys. Rev. Lett.* **95** 063004
[37] Liu J H, Jing D Y, Zhuang L, Quan W, Fang J C and Liu W M 2020 *Chin. Phys. B* **29** 043206
[38] Alcock C B, Itkin V and Horrigan M 1984 *Can. Metal. Q.* **23** 309